On the origin of microstructural discontinuities in sliding contacts: a discrete dislocation plasticity analysis

Yilun Xu[1,2*], Friederike Ruebeling[3,4], Daniel.S. Balint[1], Christian Greiner[3,4], Daniele Dini[1*]

[1] Department of Mechanical Engineering, Imperial College London, South Kensington Campus, Exhibition Road, London SW7 2AZ, UK
[2] Department of Materials, Imperial College London, South Kensington Campus, Exhibition Road, London SW7 2AZ, UK
[3] Karlsruhe Institute of Technology (KIT), Institute for Applied Materials (IAM), Kaiserstrasse 12, 76131 Karlsruhe, Germany
[4] KIT IAM-CMS MicroTribology Center (µTC), Strasse am Forum 5, 76131 Karlsruhe, Germany

Abstract

Two-dimensional discrete dislocation plasticity (DDP) calculations that simulate single crystal films bonded to a rigid substrate under sliding by a rigid sinusoid-shaped asperity are performed with various contact sizes. The contact between the thin film and the asperity is established by a preceding indentation and modelled using a cohesive zone method (CZM), whose behavior is governed by a traction-displacement relation. The emergence of microstructural changes observed in sliding tests has been interpreted as a localized lattice rotation band given rise by the dislocation activities underneath the contact. The depth of the lattice rotation band is predicted to be well commensurate with that observed in the corresponding tests. Furthermore, the dimension and magnitude of the lattice rotation band have been linked to the sliding distance and contact size. This research reveals the underpinning mechanisms for the microstructural

---

*Corresponding Author: Prof. Daniele Dini, d.dini@imperial.ac.uk Yilun Xu, yilun.xu@imperial.ac.uk

1   changes observed in the sliding tests by explicitly modelling the dislocation patterns

2   and highly localized plastic deformation of materials under various indentation and

3   sliding scenarios.

4   **Keywords:** Sliding; Discrete Dislocation Plasticity; Lattice rotation; Size effect

1   Introduction

Microstructure determines the material performance under contact, including but not limited to hardness (Chenje et al., 2004), coefficient of friction (COF) (Rigney and Hirth, 1979), anti-fretting (Zhang et al., 2009) and wear resistance (Rigney and Glaeser, 1978) under a tribological loading condition, particularly when the contact size approaches the grain size. Correspondingly, the subsurface microstructure of specimens is simultaneously changed by the plasticity induced by external tribological load that couples normal and tangential components. Therefore, it is significant to understand the mechanisms of the mutual interactions between the microstructure and the local deformation of materials under tribology loadings. Among complex tribology loading scenarios, the single asperity sliding problem provides an elementary mechanistic benchmark for revealing the mechanisms for microstructure change.

The phenomenon of microstructure variation in the sample subsurface under tribological loads has commonly been observed in experimental studies *e.g* .(Hattori et al., 2008; Hughes and Hansen, 2001; Stoyanov et al., 2014) on various crystalline metals, including nickel, copper and aluminum. Numerical investigations including the work (Karthikeyan et al., 2009; Pastewka et al., 2011) were performed to understand the intrinsic mechanisms of the subsurface modification under sliding. However, due to the complexity of the tribology contact loads, neither of the experimental nor numerical studies have not yet elucidated the phenomenon with satisfactory mechanisms. A more recent experimental study (Greiner et al., 2016) using Scanning Transmission Electron Microscopy (STEM) has shown a "dislocation traceline", *i.e.* an apparent contrast change in the STEM images within the subsurface of a copper specimen after one-stroke sliding. The abrupt contrast change was interpreted as a

1 special dislocation piling up pattern under the contact and serves as a key mechanistic

2 driver giving rise to subgrain boundary formation and further damage in subsequent

3 cyclic tribological loading (Greiner et al., 2016).

4 There are no physics-based mechanisms that have yet been proposed to provide a

5 convincing insight for the emergence of tracelines observed in sliding tests. In order to

6 interpret microstructural changes observed in the subsurface during sliding tests, a

7 previous study (Greiner et al., 2018) employed a continuum model to describe the

8 dislocation activity by assessing the inhomogeneous stress field variation under the

9 moving indenter. However, due to the lack of a length scale parameter and the discrete

10 nature of the phenomenon under investigation, neither conventional continuum

11 approaches nor crystal plasticity (*e.g.* (Dunne et al., 2007b)) is capable of capturing the

12 highly localized and discrete deformation observed in the experiments. It is in fact more

13 sensible to explicitly model dislocation activities that appear to be likely responsible

14 for the microstructural discontinuities. Hence, a 2D Discrete Dislocation Plasticity

15 (DDP) model is established in this paper to simulate the evolution of dislocations

16 motion and their pile up pattern under the sliding. The DDP numerical framework has

17 been extensively applied to provide microstructure- and length-scale associated

18 interpretation to a variety of fundamental micromechanical problems, including tension

19 (Balint et al., 2008), micro-compression (Akarapu et al., 2010) , bending (Prastiti et al.,

20 2020; Tarleton et al., 2015), nano-indentation (Qu et al., 2006) and pure sliding

21 (Deshpande et al., 2004) by simulating the activity of individual dislocations that is

22 governed by nucleation, mobility and pinning laws. In this framework, the material

23 behavior is completely determined by the collective activities of dislocations under

24 contact. The contact between the specimen and indenter that is established by a

25 preceding sinusoidal micro-indentation is modelled using a cohesive zone method

(CZM), whose shear stress performance is governed by a non-soften traction-displacement relation (Deshpande et al., 2007). We herein aim to investigate the underpinning mechanisms for local microstructural deformation and the induced lattice rotation under single asperity sliding using the DDP framework integrated with experimental observation (Ruebeling et al., 2021). The numerical results shed light on the mechanisms for the emergence of the dislocation tracelines observed in the experiment by explicitly illustrating the dislocation pilling up, geometrically necessary dislocations (GND) and consequently localized lattice rotation of the subsurface under various indentation and sliding scenarios. In addition, this research also provides a pioneering framework for simulating the localized deformation and the subsequent microstructure changes observed in the multi-cycle tribological tests, *e.g.* shown in the work (Greiner et al., 2016). The results of the analysis also benefit researchers and engineers in their pursuit of tailored and optimized the anti-wear properties of materials and coatings.

2   Methodology

2.1   Discrete Dislocation Plasticity formulation

We herein employ the classical two-dimensional, plane strain, isotropic discrete dislocation plasticity (DDP) computational framework first described by Van der Giessen and Needleman (Van der Giessen and Needleman, 1995). Although three-dimensional discrete dislocation plasticity (3D-DDD) could also be used to improve our understanding of material deformation (*e.g.* (Bertin et al., 2020; El Ters and Shehadeh, 2019; Gurrutxaga-Lerma et al., 2017; Lu et al., 2019; Motz et al., 2008)), the 2D DDP framework reflects important dislocation-related features of crystalline materials (van der Giessen et al., 2020), which can be more swiftly used to explore

1   fundamental aspects of permanent deformations and irreversible changes. The 2D DDP

2   framework adopted in this paper explicitly simulates the nucleation, glide, pinning and

3   interaction of the edge components of individual dislocation loops in crystals subject to

4   external loads and constraints assuming plane strain conditions. The formulation

5   exploits Bueckner's principle to represent the collective effect of dislocations by their

6   linear elastic superposition; plasticity arises from the irreversible, quasi-static evolution

7   of the elastic fields associated with all dislocations in the system. Hence, the localized

8   micromechanical behavior of crystalline materials (*e.g.* stress, strain and slip etc.) are

9   calculated based on the instantaneous dislocation structure induced by various loading

10   scenarios, such as tension (Balint et al., 2006b), indentation (Lu et al., 2019), shock and

11   high strain rate loading (Gurrutxaga-Lerma et al., 2017; Gurrutxaga–Lerma et al., 2020),

12   and cyclic loading (Xu et al., 2020). The essential details of the DDP framework have

13   been given in (Balint et al., 2005); only the aspects of the DDP formulation that are

14   distinct from the basic recipe are described here.

15   **2.2   The DDP model setup for sliding**

16   The basic DDP model described above is adapted here for frictional sliding problems.

17   The aim is to use the model to reproduce the experimental observation, hence enable

18   its physical interpretation. An initial sinusoidal indentation process is utilized to

19   establish contact between the rigid asperity and the specimen. This is followed by

20   monotonic sliding with a cohesive zone model (CZM) between the asperity and the

21   specimen (Deshpande et al., 2004).

22   The specimen is made of a DDP region underneath a sinusoidal asperity with an elastic

23   medium on either side, as depicted in **Figure 1**. The DDP *process window* represents a

24   single FCC-like crystal in a plane strain orientation and is assigned with aluminum-like

1 properties. Further details of the DDP parameters associated with this crystal

2 representation can be found in (Xu et al., 2016). Although the crystal representation

3 does not correspond exactly to the pure copper tested in the experiments, the similarity

4 of the slip systems ($\Phi^{(\alpha)} = 0, \pm 45°$ with respect to the x-axis in the model) to those in

5 the experiments enables mechanistic study of the microstructural change observed in

6 the sliding tests.

7 The DDP process window with dimension $l \times h$ is discretized by a finite element mesh

8 (the finite element method is used to solve the correction, or reduced problem of the

9 Bueckner linear superposition) that is highly focused towards the centre of the contact

10 area. The finite element mesh is made up of 240×100 bi-linear elements with a typical

11 mesh size of $\Delta x = 0.005$ μm in the refined zone, which has dimensions 1 μm $\times$ 1 μm.

12 A mesh-size sensitivity study was conducted, and the mesh size mentioned above was

13 found to be an optimal balance between computation expense and numerical accuracy.

14 A sufficiently-small time increment of $\Delta t = 0.5$ns was used to sufficiently resolve the

15 evolution of the dislocation structure.
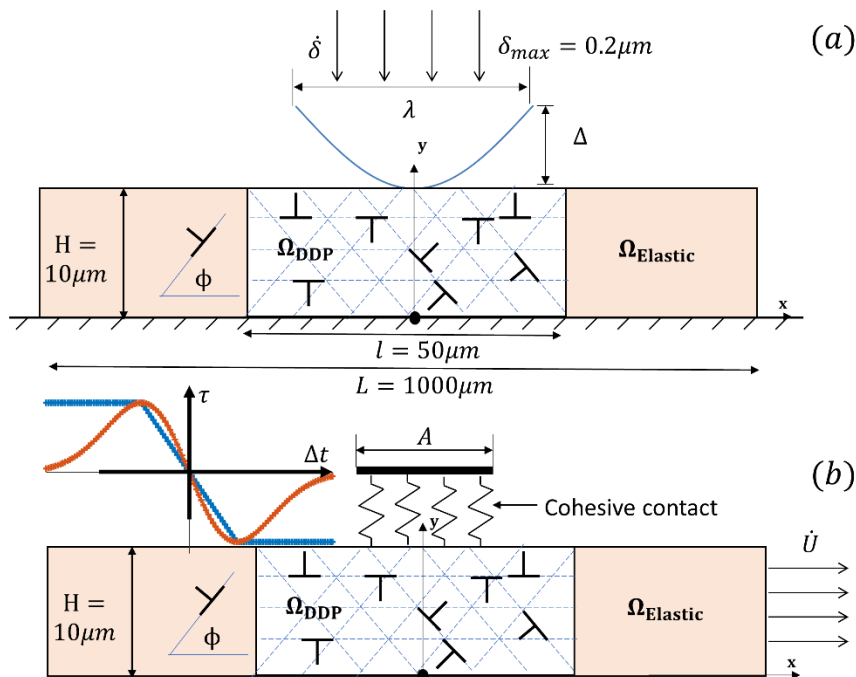
16

1   **Figure 1**. Schematic illustration of (a) the sinusoidal indentation and (b) the subsequent
2   monotonic sliding boundary value problem, solved using the DDP model.

3   Although the sinusoidal indentation model invokes a small strain approximation, the

4   contact between the indenter and film is based upon the *deformed* film surface.

5   Indentation depth is denoted by δ, and true contact length A is defined as the distance

6   between the intersections of the indenter surface and the deformed film surface. In

7   general, the true contact length A differs from the nominal contact length as material

8   sink-in or pile-up (Balint et al., 2006a) occurs. Also, nominal contact area does not

9   account for the effect of surface roughness, comprised of steps created by dislocations

10   exiting at the free surface, on the contact area, hence hardness (as analyzed and

11   discussed in (Widjaja et al., 2007a).

12   The total reaction force of the thin film response to the applied indentation depth is

13   computed as in eq. (1):

$$F = - \int_{-A/2}^{A/2} T_y(x, H)\, dx \tag{1}$$

14   where T_y is the surface traction in the *y*-direction, hence the indentation pressure (*i.e.*

15   instantaneous or indentation depth-dependent hardness) *p* is defined by:

$$p \equiv F/A \tag{2}$$

16   where A is the actual, end-to-end length definition of the contact area.

17   The interaction between surfaces can be modelled by applying a continuum cohesive

18   formula (Johnson, 1997). In the sliding simulations, the interaction between the

19   sinusoidal asperity and the specimen is modelled using a cohesive zone on the

20   contacting surface of length A with a relation between shear traction versus

21   displacement, which is given by:

$$T_t = \begin{cases} -\tau_{max}\dfrac{\Delta t}{\delta_t}, & \text{if } |\Delta t| < \delta_t \\ -\tau_{max}sign(\Delta t), & \text{if } |\Delta t| > \delta_t \end{cases} \tag{3}$$

1 where $\Delta t = u_x(x, H)$ is the tangential displacement jump across the cohesive surface,

2 and $T_t = T_x$ is the shear traction. Hence, the interaction is a cohesive resistance to the

3 relative sliding of the thin film, here chosen to be represented by a "non-softening"

4 cohesive relation with unbounded shear work of separation (Deshpande et al., 2004).

5 While there is at present no fundamental basis for choosing the form of cohesive

6 relation to use in conjunction with the discrete dislocation description of material

7 behavior, the interaction between adhesion and tangential tractions is in itself currently

8 at the center of an active scientific debate (see *e.g.* (Menga et al., 2018; Peng et al.,

9 2021)) and very much depends on the nature of the specific interfacial characteristics

10 of the contact pair being investigated. In addition, the cohesive law chosen in our study

11 helps the convergence of contact calculations, and hence has been commonly used in

12 other sliding studies, such as (Deshpande et al., 2007; Song et al., 2016).

13 Traction free boundary conditions are applied on the part of the surface outside of the

14 contact region:

$$T_x = T_y = 0 \text{ on } x = 0 \notin S_{contact} \text{ and } y = H \tag{4}$$

15 The maximum cohesive strength τ_{max} is set to be τ_{max}=300MPa and the threshold

16 displacement jump is δ_t = 0.5nm. The parameter values in the non-softening traction-

17 displacement relation are identical to (Deshpande et al., 2007)).

18 The displacement rates,

$$\dot{U}_x = \dot{U}, \dot{U}_y = 0 \tag{5}$$

19 are imposed on the specimen boundaries $x=\pm L/2$, and $y=0$, to simulate the relative

20 sliding of the specimen with respect to the contact surface with magnitude $\dot{U}/A =$

1   $10^4 s^{-1}$ in the positive *x*-direction. The maximum sliding distance is set as

2   approximately one half of the corresponding contact size *A*, which is sufficiently large

3   to achieve a full slip condition (see the later discussion in Section 3.2) of the film. The

4   sliding rate $\dot{U}$ was chosen sufficiently low to ensure a quasi-static sliding process, *i.e.*

5   that dislocations are in an equilibrium configuration at any sliding instance, hence the

6   effect of loading rate on sliding (due to nucleation time and mobility as shown in (Song

7   et al., 2016) is negligible. The averaged shear stress τ along the contact is given by:

$$\tau = -\frac{1}{A} \int_{-A/2}^{A/2} T_x(x, H)dx \tag{6}$$

8   Different from the pure sliding calculations where films are assigned with a dislocation-

9   and stress-free initial state using the DDP framework, *e.g.* (Benzerga, 2008)), the

10   sliding simulations herein start with a certain normal load and actual contact size to

11   accommodate the experimental setup. In fact, this type of sliding calculation is initiated

12   with a deformation field and dislocation structure in the specimen that is introduced

13   from the initial sinusoidal indentation simulations described above, with varying

14   indentation depth.

15   **2.3   Lattice rotation calculation**

16   We use the DDP framework described above to model the microstructural change, more

17   specifically, the elastic lattice rotation within the thin film under frictional sliding

18   scenarios. The lattice rotation is defined as the antisymmetric part of the displacement

19   gradient tensor, which for the planar situation can be expressed in terms of the off-

20   diagonal components of the small strain tenor ϵ_{ij}. Therefore, lattice rotation is

21   comprised of the derivatives of the displacements in the infinite plane discrete

22   dislocation field and ($\tilde{}$) and the continuum correction field ($\hat{}$) :

$$\Omega = \frac{1}{2}(\hat{u}_{2,1} + \tilde{u}_{2,1} - \hat{u}_{1,2} - \tilde{u}_{1,2}) \tag{7}$$

1   The DDP model considers only glide of edge type dislocations along predefined slip

2   systems within the material, which introduce slip (displacement discontinuities) across

3   the slip planes. A cluster of dislocations piling up introduces lattice rotation to the

4   material. This phenomenon has also been reported in indentation problems (Balint et

5   al., 2006a; Po et al., 2019; Zhang et al., 2014). Displacement discontinuities should not

6   appear in the derivatives of the displacements, they are continuous, however this

7   requires analytical differentiation. Standard numerical differentiation of the dislocation

8   displacement fields will reveal a discontinuity, a fact that is often exploited for

9   visualization of slip localization (Hirth and Lothe, 1982). Hence when computed in this

10 way, the definition of lattice rotation Ω in eq. (7) naturally excludes slip features from

11 the ($\tilde{}$) field

12 In principle, we can employ a different background mesh, using interpolation, that is

13 different from the finite element mesh used in the calculation in order to change the

14 resolution of field quantities. In this work we resolve field quantities on the highly

15 focused mesh used in the simulation to maintain their spatial resolution in the vicinity

16 of the indentation, especially near the contact surface. The lattice rotation calculation

17 was performed every 100 times increments, *i.e.* $\Delta U/A = 5 \times 10^{-4}$, to capture the

18 temporal evolution of lattice rotation against sliding distance.

19 The aforementioned elastic lattice rotation method was verified for a wedge-shaped

20 indentation problem; a comparison to prior simulations (such as (Zhang et al., 2014)))

21 is shown in the Appendix. The abrupt change in the sign of the lattice rotation near the

22 midline of the contact is consistent with experimental observations ((Kysar et al., 2010)

and continuum plasticity analyses ((Bouvier and Needleman, 2006). The values of lattice rotation predicted here are also consistent with (Zhang et al., 2014)). It is worth noting that the lattice rotation distribution is obtained by the combined effect (linear superposition of fields) of dislocations on the three slip systems, and the lattice rotation caused by isolated dislocations is long range. Therefore, the lattice rotation distribution shows a different pattern from the corresponding dislocation distribution, since the rotations caused by isolated, moving dislocations is experienced far from the dislocations themselves; in other words, regions with a high value of dislocation density do not necessarily exhibit a hot spot of lattice rotation. This phenomenon is further illustrated and discussed when looking at the evolution of lattice rotation contours and dislocation structure in the following sections (see *e.g.* **Figure 9**).

3 Numerical results

3.1 Sinusoidal indentation response

The variation of actual indentation pressure p_A and actual indentation contact area A against applied indentation depth δ under the rigid sinusoidal asperity with an amplitude $\Delta = 0.5\mu m$ and wavelength $\lambda = 10\mu m$ are reported in **Figure 2**. The indentation pressure does not exhibit a strong indentation size effect (ISE) response, consistent with micro-indentation tests (Kuksenko et al., 2019; Pharr et al., 2010) and numerical simulations (Balint et al., 2006a; Lewandowski and Stupkiewicz, 2018; Saraev and Miller, 2006), when the indentation depth exceeds $\delta = 0.02\mu m$. The presence of an ISE requires a high strain gradient in the plastically deforming volume under the indenter (Nix and Gao, 1998), accommodated by a high density of geometrical necessary dislocations (GNDs). However, the relatively blunt, smooth surface of the sinusoidal indenter (e.g. compared to a wedge) used here suppresses the development of the strain gradient when indentation depth is sufficiently large ($\delta >$

1    $0.02\mu m$), and the actual indentation pressure response stabilizes at a plateau level that

2   represents the continuum hardness of the specimen. The hardness value predicted here,

3    $p_A \cong 210\text{MPa}$, is reasonably close to the continuum plasticity prediction, $p_A = 3\sigma_Y$,

4   which establishes that plastic flow dominates the specimen response under sinusoidal

5   indentation with a large contact size. The size-insensitive indentation pressure regime

6   is useful in understanding the shear stress response in later sliding calculations by

7   excluding the normal stress interference. Compared to the nominal contact size (dashed

8   line in **Figure 2**), the actual contact size systematically exhibits a smaller value by

9   virtue of the material sink-in near the contact, which was observed in prior DDP

10   analyses of indentation (Widjaja et al., 2007b; Xu et al., 2019).
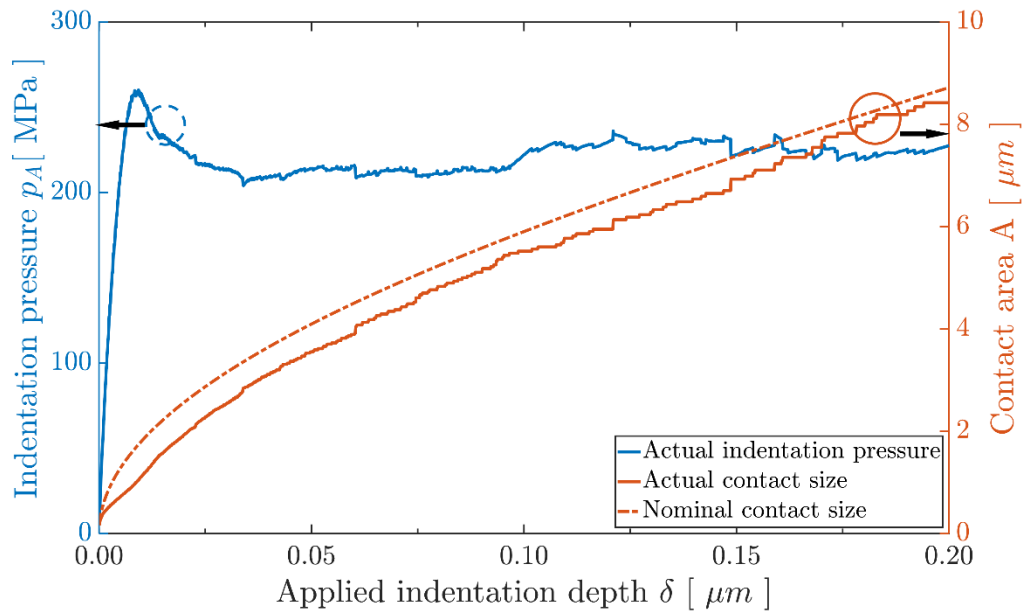
11

12   **Figure 2**. Actual indentation pressure p_A and actual contact size A versus applied
13   indentation depth δ by the sinusoidal asperity with $\lambda = 10\mu m$ and $\Delta = 0.5\mu m$. The
14   nominal contact size A_N (denoted by the dash-dot line) response is also included for
15   comparison.

16   **3.2   Subsurface deformation at different stages during sliding**

17   The evolution of the average shear stress τ_{avg} along the contact with the sliding

18   distance U is reported in **Figure 3** using the DDP model. The results were obtained

1   from sliding simulations starting from four different initial indentation depths, $\delta =$

2     $0.01, 0.05, 0.10, 0.20\mu m$, with a sinusoidal asperity shape with $\lambda = 10\mu m$ and $\Delta =$

3     $0.5\mu m$, and the corresponding actual contact sizes $A = 1.11, 3.55, 5.52, 8.42\mu m$,

4   respectively, were achieve by the initial indentation. Following an initial linear response,

5   the evolution curves continue to increase but with a much slower and strongly contact

6   size dominated rate $\partial \tau / \partial A$ until the cohesive strength τ_{max} is achieved. It can be

7   observed that the critical sliding distance for the average shear stress achieving the

8   cohesive strength depends on the contact size. In previous studies on sliding

9   calculations without a prior indentation, the shear stress was found to be inversely

10   square root dependent on the contact size (Deshpande et al., 2007). The preceding

11   sinusoidal indentation in this research introduces considerable plasticity into the film

12   prior to the sliding, therefore the relationship revealed under pure sliding does not hold

13   when indentation is first applied. The quantitative relation between the shear stress

14   increase with the initial indentation and the contact size will be investigated in detail in

15   future studies.

16   The total dislocation density ρ_{dis} (number of dislocations divided by the area of the

17   dislocation process window) evolution with the sliding distance U is reported in **Figure**

18   **4**, where results were obtained from the aforementioned DDP simulations for four

19   different contact sizes. The total dislocation density linearly increases from a base value

20   that was inherited from the preceding indentation. The rate of increase in the dislocation

21   density is found to be independent of contact size.
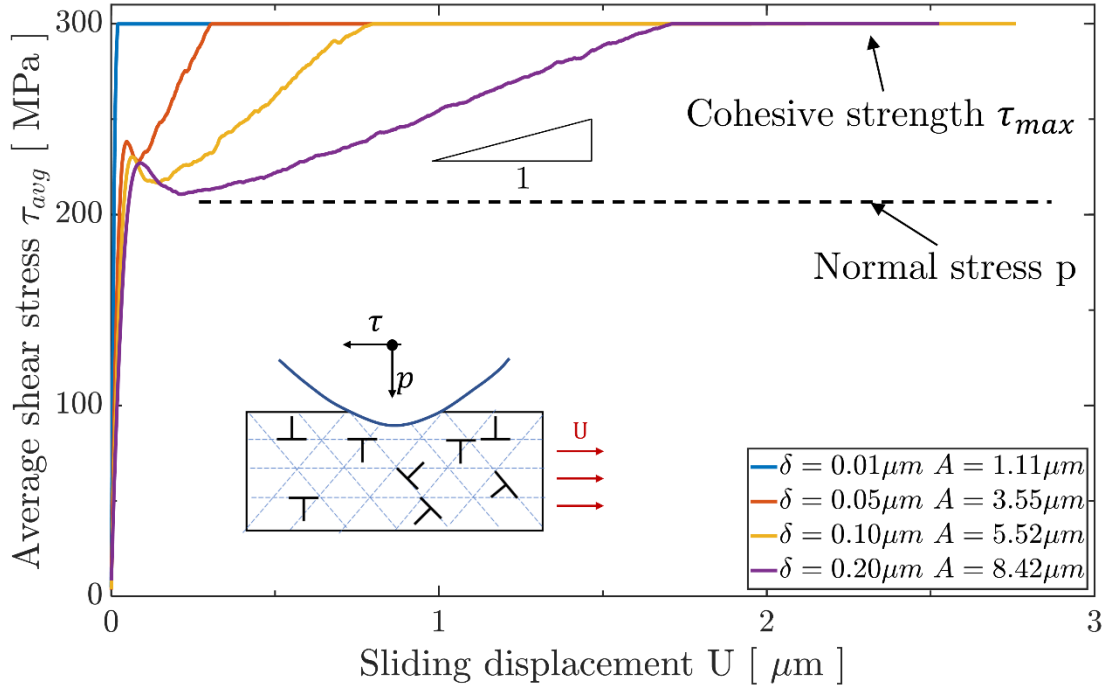
Figure 3. Shear stress τ evolution with sliding displacement U for four different contact sizes that are introduced by initial sinusoidal indentation. The normal stress p and cohesive strength τ_{max} are denoted for reference.

After a critical sliding distance, the rate of increase is reduced for all contact sizes, when more plasticity is introduced into the specimen by virtue of the increased sliding load; the critical sliding distance at which this occurs strongly depends on the contact size, and is greater than the critical sliding distance at which the average shear stress achieves the cohesive strength for a given contact size (see **Figure 3**). For instance, the critical sliding distances are predicted as 1.0μm and 0.76μm for the dislocation density evolution and shear stress evolution, respectively, for a contact size A = 5.52μm. The dislocation density eventually reaches a plateau value (except for the largest contact size A = 8.42μm), which is determined by the contact size, and ceases to increase with sliding distance. This suggests that the film is saturated by a stable dislocation structure, therefore full slip between the contact and specimen occurs.
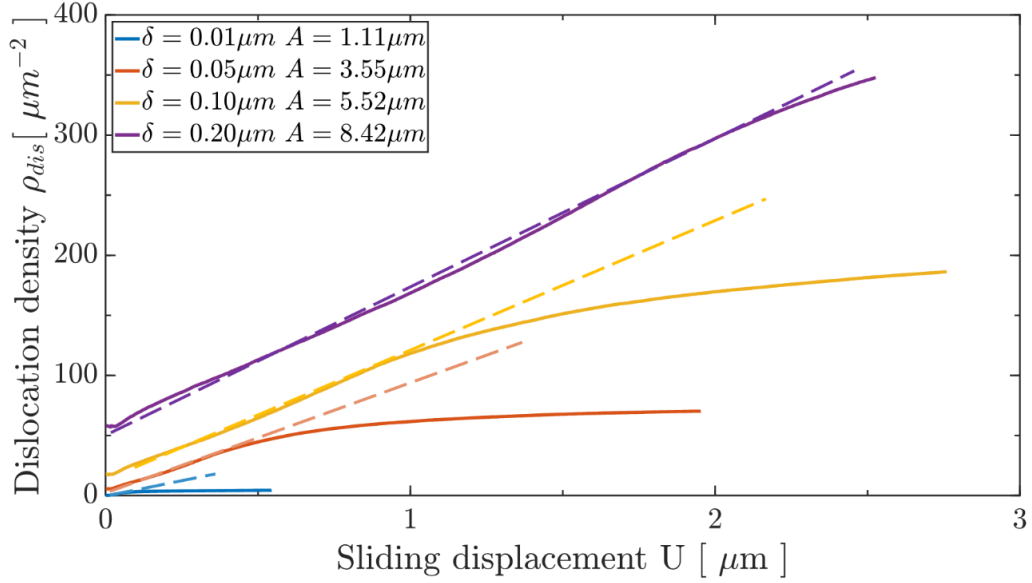
Figure 4. Total dislocation density ρ_{dis} evolution against sliding displacement U under different contact sizes introduced by an initial sinusoidal indentation. The dashed lines indicate the contact-size independent dislocation density increase rate prior to full slip occurring.

Hence, three different sliding stages are identified, demarcated by the two aforementioned critical sliding distances for a given contact size. While the average shear stress evolution reflects plastic flow due to dislocation activity within the surface region (Deshpande et al., 2004, 2005) only, the dislocation density evolution is able to identify the point at which the full slip state initiates, *i.e.* when the dislocation structure and deformation field within the entire specimen reach a dynamic equilibrium and the dislocation density tends to saturate as sliding takes place. In the following sections, lattice rotation maps in the whole specimen are analyzed at different sliding stages for various contact sizes.

3.3   Lattice rotation evolution during sliding

The lattice rotation is calculated using eq. (7) according to the dislocation structure and deformation field at a certain instant of a sliding process. The evolution of the lattice rotation distribution for the contact size A = 3.55 µm for single-stroke (left to right) sliding is illustrated in **Figure 5** with individual dislocations shown explicitly as black

1   marks; a view of the entire specimen is shown above a close-up view of the

2   10μm × 1μm dashed region shown. With increase in sliding distance the lattice

3   rotation accumulates underneath and behind the contact. In particular, it is shown that

4   the lattice rotation introduced by the indentation that precedes sliding is negligible

5   compared to that induced by the sliding itself. As shown in (c) and (d), after sufficient

6   sliding the lattice rotation in a thin layer of material immediately underneath the contact

7   with thickness $h^* \approx 100$ nm has its lattice rotation 'locked in', i.e. it does not increase

8   in intensity but does spread with further sliding.
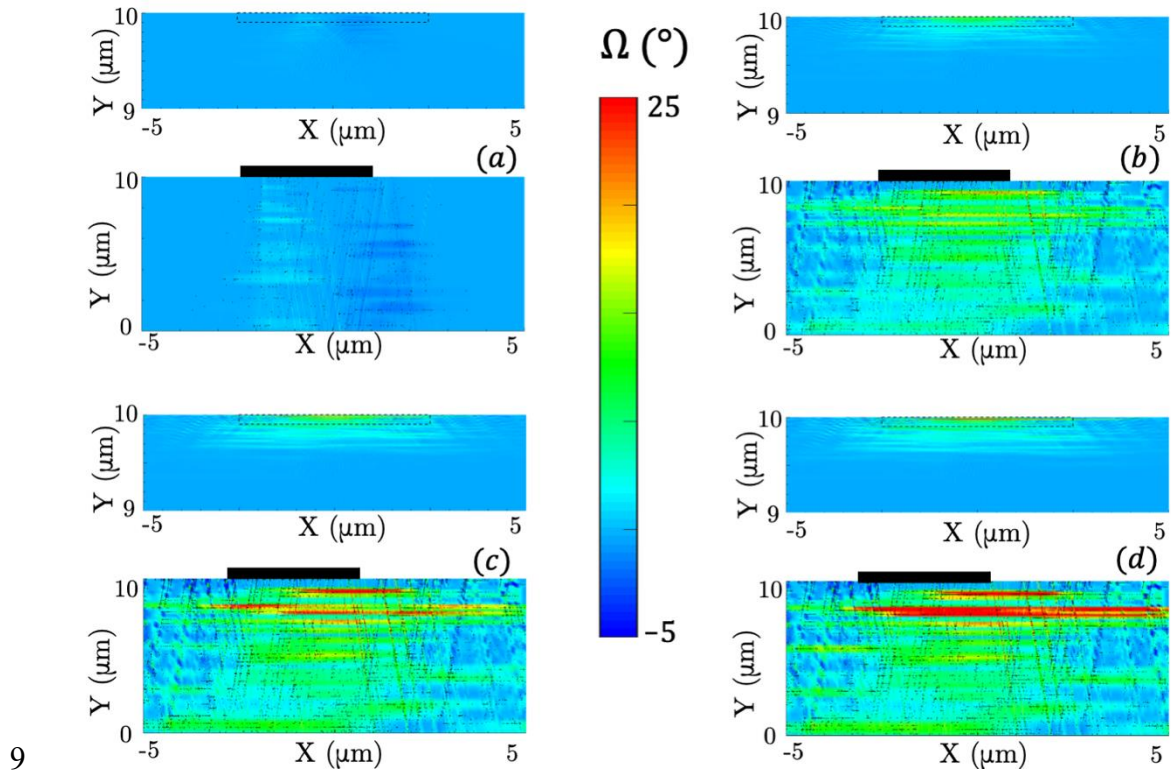
10 **Figure 5**. The contours of lattice rotation Ω and the corresponding dislocation
11 structures (individual dislocations represented as black dots) of the sliding calculation
12 starting from $\delta = 0.05$ μm and $A = 3.55$ μm. Results are shown for sliding distances
13 (a) $U = 0$ (i.e. just after indentation), (b) $U = 0.497$ μm (the initial slip), (c) $U =$
14 1.561 μm (partial slip) and (d) $U = 1.953$ μm (full sliding), where U is the relative
15 surface displacement, A the contact size and δ the indentation depth. The set of lattice
16 rotation contours with corresponding dislocation structures illustrate the emergence of
17 the 'locked-in' and localized lattice rotation bands during the sliding process.

18   This is accompanied by localization of lattice rotation in a thin band beneath this layer,

19   which spreads parallel to the sliding direction and increases in strength as the sliding

1 distance increases. More bands of localized lattice rotation with associated 'locked-in'

2 layers are visible with increasing distance below the surface, particularly once the full

3 sliding conditions are achieved (**Figure 5(d)**). The 'locked-in' lattice rotation bands

4 correspond to the trace lines experimentally observed in (Greiner et al., 2016; Greiner

5 et al., 2018), where the localization band is the boundary between them.

6 Lattice rotation within a single crystal material is associated with the presence of

7 geometrically necessary dislocations (GNDs) (Arsenlis and Parks, 1999),

8 microstructure change (Cheng and Ghosh, 2015; Cheong et al., 2005; Das et al., 2018;

9 Dunne et al., 2007a) and non-local effect (Counts et al., 2008; Meissonnier et al., 2001).

10 The results shown in the following sections correspond to sliding distances that exceed

11 that required for the full sliding condition, beyond which the layered lattice rotation

12 distribution depicted in **Figure 5** is fully developed.

13 **3.4   Contact size effect on lattice rotation**

14 The contact size plays a crucial role (Deshpande et al., 2007; Liu et al., 2018) as it

15 strongly affects the plasticity introduced into the specimen. Besides the shear stress and

16 dislocation density reported in previous sections, the localized lattice rotation band and

17 the 'locked-in' layer, henceforth referred to as a trace line to be consistent with the

18 experiments, are illustrated for different contact sizes in **Figure 6**. As expected, a larger

19 contact size produces a dislocation structure with a larger number of dislocations, which

20 propagate much deeper into the indented material; this is also associated with the

21 formation of more than one trace line. However, the location and intensity of the trace

22 lines is nearly independent of the contact size, at least for smaller contact sizes, which

23 correspond to smaller loads in the experiments. Of more significance, the depth from

24 the surface of the first trace line is also independent of the contact size. This is consistent

25 with experiments (Greiner et al., 2016).
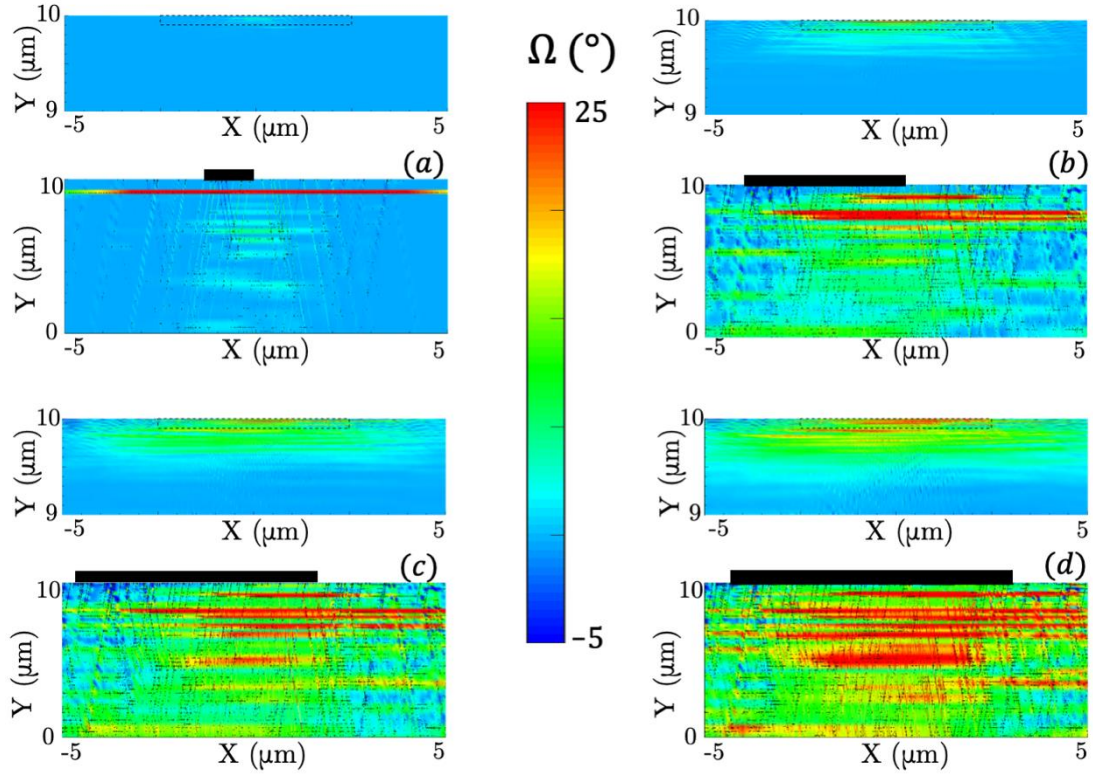
Figure 6. The contours of lattice rotation Ω and the corresponding dislocation structure (individual dislocations represented as black dots) of the sliding calculation obtained for different contact sizes. (a) $A = 1.11\,\mu m$, (b) $A = 3.55\,\mu m$, (c) $A = 5.52\,\mu m$ and (d) $A = 8.42\,\mu m$, where U is the displacement, A the contact size and δ the indentation depth. Results are shown at the instants where full sliding has been achieved for each contact size and the indenter has moved away from the initial contact area (a, b and c), or for the maximum sliding distance the calculation has reached (d). The set of lattice rotation contours illustrates the lattice rotation bands formed during sliding and the contact size effect on lattice rotation band.

Figure 7 illustrates the three characteristic dimensions of the trace lines revealed in the specimen subsurface under contact size $A = 3.55\mu m$, which exhibits features representative of all contact sizes. The critical depth h^* indicates the distance between the surface and the boundary between the first and second trace lines, which is independent of contact size. The critical depth is predicted by the DDP model for all contact sizes as $h^* = 0.09\,\mu m$, which is comparable to the experimental finding of $0.1\,\mu m$ (Greiner et al., 2016). This corresponds to a highly localized deformation, which is also what characterizes the depth of the plastic zone (represented as plastic slip zone), which varies as a function of the contact size and is computed to be 1.2, 3.5, 5.2

1   and 7.6 µm for the four contact sizes analyzed here, respectively. It has been verified

2   that the tracelines predicted by the DDP simulation are not mesh or slip plane spacing

3   dependent, and are not an artefact of the choice of contour levels; the mesh was fine

4   and highly focused to the surface with a mesh size as small as $0.01 \mu m$, and dislocation

5   activity was observed between the first trace line and the contact. Both the width and

6   height of the group of trace lines, referred to here as the lattice rotation band, labelled

7   dl and dh, are determined by the plasticity, hence by the contact size of the preceding

8   indentation. In the case shown here, the width of the lattice rotation band is measured

9   as $dl = 9.5 \mu m$ and the height as $dh = 6 \mu m$. In the experiments the contact size was as

10   large as $92 \mu m$, much larger than in the simulations presented here (Greiner et al., 2016;

11   Liu et al., 2018). However, as shown in **Figure 7**, dl and dh scale with the contact size,

12   therefore it is expected that the dimensions predicted by the DDP simulations would be

13   consistent with the experimental findings for much larger contact sizes.
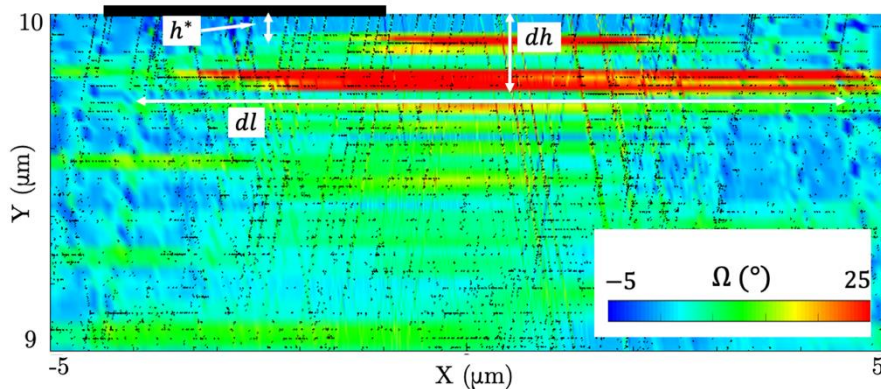
14

15   **Figure 7**. Characterization of the lattice rotation band for $U = 2.76$ µm and contact
16   size A = 3.55µm. The condition of full sliding has been reached.

17   **4   Discussion**

18   **4.1   The origin of the lattice rotation band within the subsurface**

19   It is not yet understood how the experimentally observed dislocation trace line(s)

20   originate from the dislocation structure induced by the sliding process (Greiner et al.,

1 2018). In the discrete dislocation plasticity calculations (**Figure 5** and **Figure 6**), the

2 resolved shear stress is highest on the slip system parallel to the sliding direction (*i.e.*

3 parallel to the *x*-axis) on the planes nearest to the surface, hence it is reasonable to

4 anticipate that dislocation activity on these slip planes is responsible for the observed

5 tracelines. As a result of the cohesive sliding boundary condition, the subsurface

6 material would like to assume a simple-shear, stack-of-cards like slip arrangement

7 (Haug et al., 2020); however compatibility with the surrounding bulk material prevents

8 that from happening perfectly, which results in a corresponding lattice rotation. The

9 mechanisms that the lattice rotation is given rise by accumulative dislocation glide and

10 crystalline slip due to geometry and boundary constraints have recently been observed

11 in other independent experimental observations including high-resolution digital image

12 correlation (HR-DIC) (Sperry et al., 2020) and high-resolution Electron backscatter

13 diffraction (HR-EBSD) (Maj et al., 2020), respectively.

14 To illustrate the origin of the dislocation traceline, the degree of rotation in the lattice

15 rotation band is plotted versus horizontal position *x* for contact size A $=$ 1.11 μm

16 under a full slip condition in **Figure 9**, for both vertical extents of the band identified

17 from the lattice rotation contour plot (paths B-B' and C-C'); the width of the lattice

18 rotation band observed from the lattice rotation contour plot is dependent on the cut-off

19 value that is chosen, as shown in the figure. In the inset to **Figure 9**, it is evident that

20 dislocation dipoles pile up in queues on a single horizontal slip plane underneath the

21 contact, which are driven apart by the applied shear stress. The gradient in resolved

22 shear stress on that slip plane – it is largest at the center of the contact and decays to

23 zero far away from the cohesive sliding boundary condition – causes a 'soft' pile-up to

24 form. The lattice rotation at a point on the slip plane of a single dislocation dipole is

25 zero outside the dipole and a constant value anywhere within the dipole. Hence,

1   theoretically, an arrangement of concentric dipoles creates a lattice rotation profile on

2   the active slip plane that is largest at its center and decreases incrementally moving

3   outward. This is what is observed in **Figure 9**, where fluctuations from the theoretical

4   trend are caused by dislocations on other slip planes.
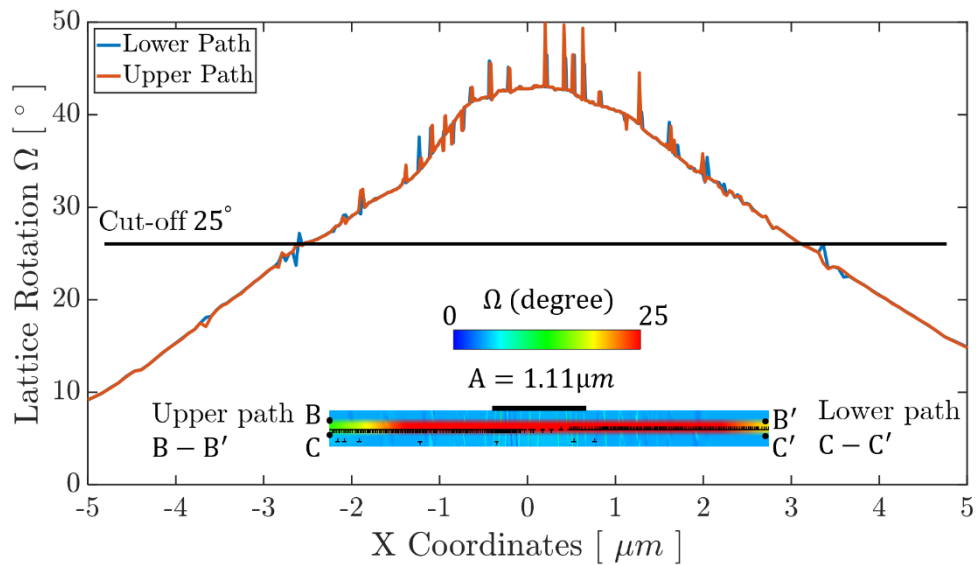
5

6   **Figure 8.** Lattice rotation on a horizontal slip plane within the subsurface. Results are
7   shown when full slip is achieved for contact size A $=$ 1.11 μm (see **Figure 6**a).

8   The instantaneous dislocation structure, corresponding GND density distribution and

9   lattice rotation distribution within the specimen for a contact size A $=$ 1.11 μm under

10   a full slip condition is reported in **Figure 9**(a), (b) and (c), respectively. Dislocations

11   on the horizonal slip system, which are the key contributors to the lattice rotation, are

12   identified by a dislocation symbol that is twice as large as those on the other slip systems.

13   Localized GND density is calculated using the net open burger's vector algorithm based

14   on the instantaneous dislocation structure (Kiener et al., 2011). A Burgers circuit size

15   of 25nm was found to adequately resolve the GND distribution for these simulations.

16   A strip of high GND density (**Figure 9**(b)) is identified in the same location as the

17   lattice rotation band, which also correlates spatially with the 'soft' pile-ups of

18   concentric dislocation dipoles on horizontal slip planes identified here as the cause of

1 the experimental STEM observations of dislocation tracelines (Greiner et al., 2016);

2 furthermore, the magnitude of the predicted GND density is in line with previous

3 measurements performed in sliding tests (Greiner et al., 2016; Greiner et al., 2018).

4 Regions of low lattice rotation, particularly that of the region between the lattice

5 rotation band and the surface, referred to here as a 'locked-in' layer, also correlate with

6 low GND density as observed in the experiments.
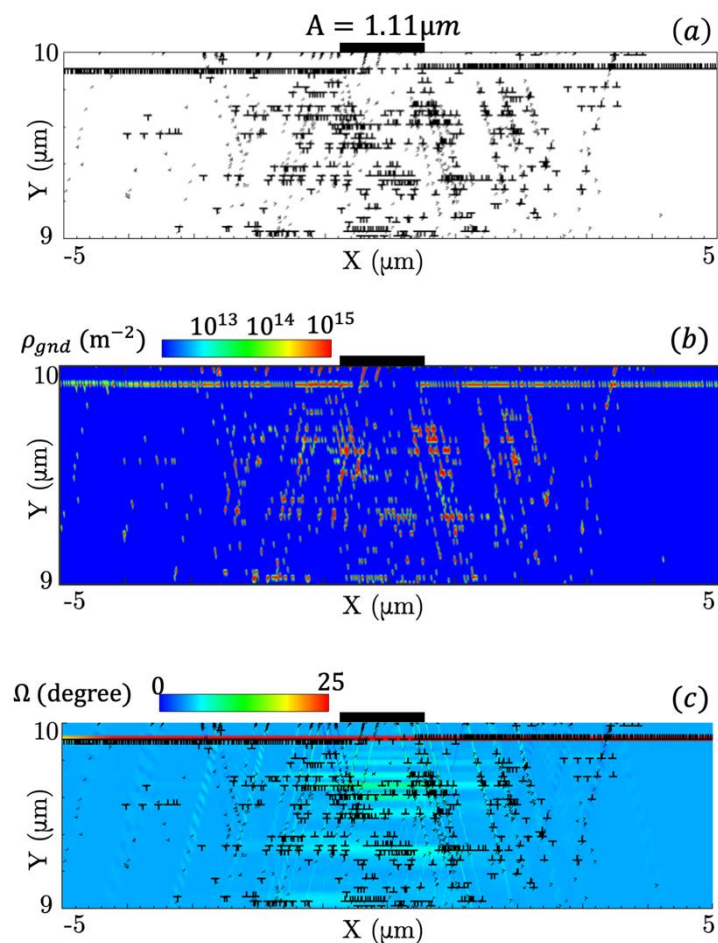
7

8 **Figure 9**. Correlation between (a) the instantaneous distribution of dislocations, (b) the
9 corresponding geometrically necessary dislocation (GND) density distribution and (c)
10 lattice rotation using the discrete dislocation plasticity model. Numerical results are
11 extracted when full sliding occurs under contact size A = 1.11μm (see **Figure 6**a).
12 Dislocation symbol size is enlarged for dislocations along the horizontal slip planes.

13 **4.2   Comparison between STEM measurements and DDP simulation results**

14 In the numerical results shown in Sections 3.3 and 3.4, the emergence of the

15 experimentally observed dislocation traceline is interpreted as a result of the formation

of queues of dislocation dipoles, or soft pile-ups, on slip systems parallel to the sliding direction. In this section, we compare STEM images, which show the contrast corresponding to microstructure change under sliding tests, and the lattice rotation contours obtained in the simulations. A typical comparison between experiments and simulations is illustrated in **Figure 10**(a). Since the appearance of the first (uppermost) traceline is common to all indenter sizes as shown in **Figure 9**, the lattice rotation is post-processed from the simulation with contact size $A = 1.11$ μm after full slip has developed and the dislocation structure has evolved to its final configuration, as this case best illustrates the mechanism responsible for the traceline and its link to lattice rotation. As mentioned previously, the simulations clearly identify a region about 0.1 μm under the contact surface where a large number of dislocation dipoles glide parallel to the surface, and a corresponding layer above it which is 'locked-in' and does not deform appreciably. The lattice rotation along three vertical paths (defined in (a)) originating at the contact face are shown in **Figure 10**(b). A significant peak indicating very large lattice rotation is observed about 0.1 microns from the contact surface. This peak diminishes moving from the contact center (the blue path) towards the contact edge (the green path), which reflects the results in **Figure 8**. The vertical distribution of lattice rotation divides the material into three layers, moving from the contact face into the bulk. These are: a rotation-constrained zone, a region with significant lattice rotation (due to soft pile-ups of dislocations on horizontal slip planes) and a remote zone that is unaffected by the sliding. This dislocation configuration in conjunction with the contact constraint induces large localised lattice rotation, interpreted physically as a line (in fact, a very thin layer of material) parallel to the sliding direction across which there is an abrupt change of microstructure, as observed in the experiments. This is in strong agreement with the evidence provided by the companion paper that the

1   misorientation is concentrated at the DTL (see e.g. Figure 6 of (Ruebeling et al., 2021)

2   and related discussion). This magnitude of the characteristic length is system specific

3   and we believe is linked to the combined effect of the cohesive strength (i.e. maximum

4   shear stress), Burger's vector and other material properties (moduli, plastic flow stress)

5   used to describe the specific systems under investigation. The nature of the load and the

6   contact size affect the behaviour (and the relative lattice rotation/deformation) of the

7   material above and below the DTL, as discussed below in more details.
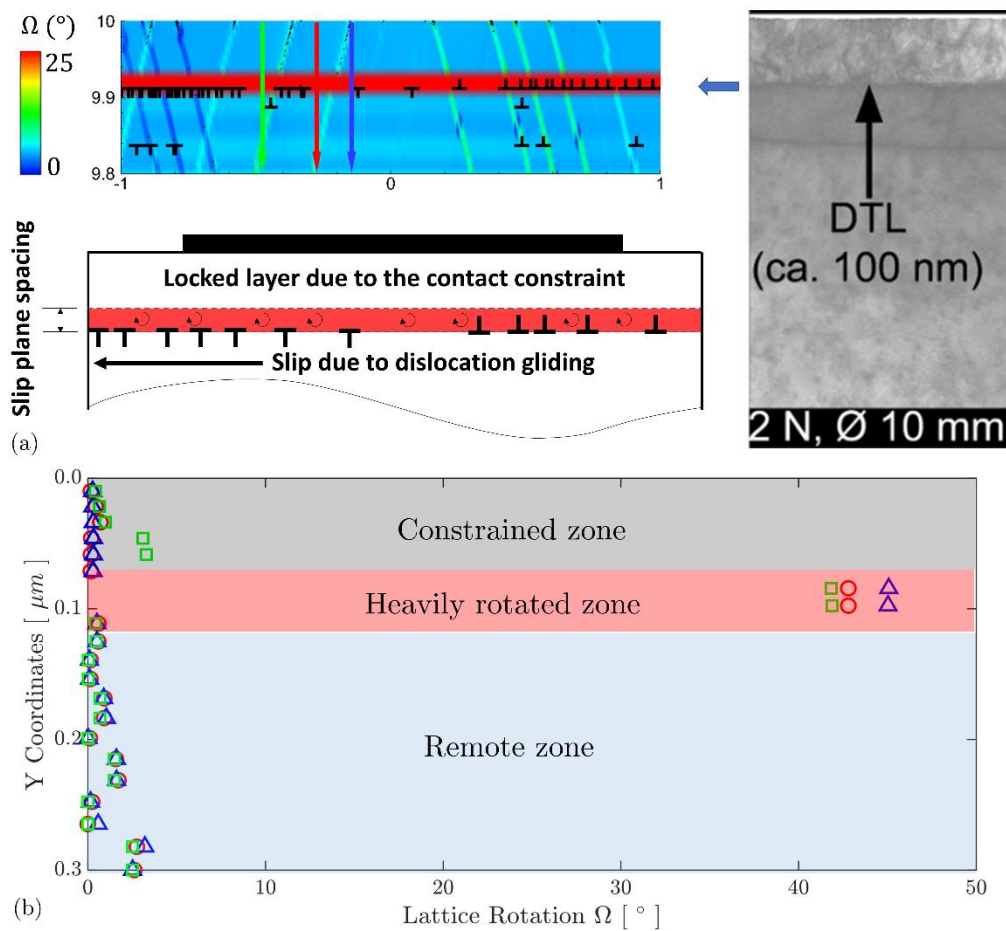
8

9   **Figure 10**. (a) Comparison between the STEM image obtained from experiments for
10 low loads (shown on the right, zoomed-in from **Figure 6**a) and the lattice rotation and
11 superimposed dislocation structure computed via DDP simulations (shown on the top-
12 left, zoomed-in from Figure 9a), highlighting the dislocation activity linked to the
13 mechanism responsible for the lattice rotation and formation of the traceline. This is
14 also schematically depicted at the bottom-left, showing the (b) lattice rotation
15 distribution along three paths (defined in (a)) perpendicular to the sliding direction.
16 Results are shown at the instant when the sliding has been initiated and dislocation
17 motion has developed in the slip systems underneath the contact.

1 The critical depth of the 1st DTL obtained from the simulations (0.1 μm) agrees very

2 well with the experimental findings, albeit the contact size in the two was different but

3 this feature was shown in the simulations to be contact-size independent; the dislocation

4 activity under the indenter is strictly controlled by the pressure and the shear traction

5 transmitted across the interface, which is an approximate match between the

6 simulations and the values experienced by the material layer under low loads in the

7 experiments. Changing the size of the indenter changes the extent of the material

8 affected by large stresses rather than the value in the uppermost layer of the material.

9 The features shown in **Figure 10** are common to all other indentation sizes but extend

10 further into the specimens for larger indenters, with the emergence of other tracelines

11 (as also shown in the experiments) further away from the surface. The dislocation

12 activity becomes more complex when the indenter size (and hence the overall load since

13 the pressure on the indenter in the experiments is kept constant) grows due to the

14 activation of a large number of dislocations along different slip systems and slip planes.

15 This usually results in progressive material rotation between tracelines (i.e. bands

16 increasing in lattice rotation between consecutive DTLs), with the largest lattice

17 rotation experienced by the plastically deformed material further away from the contact;

18 this is due to the fact that this region, which one can associate with the bulk material

19 (see **Figure 6**), in not constrained by the indenter and lattice rotation exhibits itself

20 differently in this region. This explains not only why the number of DTLs and the lattice

21 rotation increase with the size of the indenter, but also why large contact areas (typical

22 of the experiments under consideration) result is large lattice rotations recorded beneath

23 the last observable DTL, as the reach of the plastically deformed area is much deeper

24 than the area analyzed by STEM. A further interesting point to discuss is that increasing

25 the load leads to more severe microstructural changes, which include increased

1 (geometrically necessary) dislocation activity (and hence damage(Lu et al., 2020)) and

2 the formation of small grains and re-crystallization in the tribologically affected layer.

3 The simulations in **Figure 6**(d) (largest indenter size studied here) already show very

4 large dislocation activity on different slip systems. It can be inferred that a large contact

5 size and normal load may lead to the subsequent formation of new grain boundaries

6 GND density that have been characterized in previous experiments (Greiner et al.,

7 2016).

8 **4.3   Comparison between TKD measurements and DDP simulation results**

9 The qualitative comparison between the STEM image and the lattice rotation contours

10 in **Figure 10** has shown the strong correlation between the perceived abrupt

11 microstructural changes in the experiments and the material lattice rotation under

12 sliding conditions. We turn now to quantitative measurements using Transmission

13 Kikuchi Diffraction (TKD), which have been used to determine lattice rotation in the

14 neighborhoods of the DTLs in (Ruebeling et al., 2021).
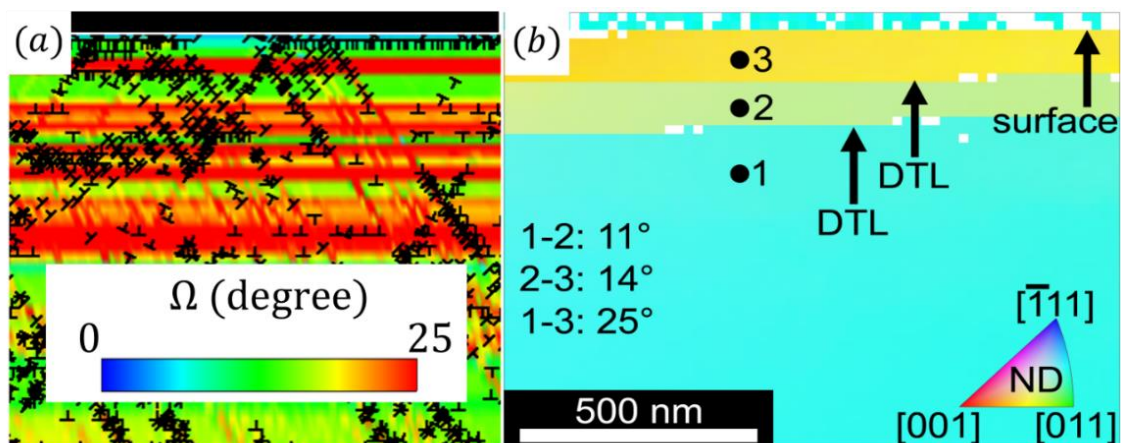
15

16 **Figure 11**. The comparison between (a) lattice rotation evaluated in DDP simulations
17 with superimposed instantaneous dislocation structure and (b) lattice rotation measured
18 using the TKD pattern. Numerical results are shown for full slip and contact size A =
19 95μm, when dislocation motion and lattice rotation have reached their final stable
20 configuration. The simulation set-up is the closest possible scenario to replicate the one-
21 stroke sliding tests.

1   The lattice rotation within the specimen calculated using DDP and measured using TKD

2   is illustrated in **Figure 11** (a) and (b), respectively. The numerical results in **Figure 11**

3   (a) are obtained from simulations under the maximum contact size ($A = 95\,\mu m$)

4   achieved in the DDP calculations, which is the closest match possible between the two

5   systems given the computational demands of DDP. The subsurface region under the

6   indenter is subjected to a similar stress state. However, the size of the indenter used in

7   the simulation is still smaller than the contact area for the equivalent experiment, hence

8   the region of material over which high stresses and strains are calculated is not as deep

9   as the equivalent region in the experimental test. The $A = 95\,\mu m$ simulation is

10   nonetheless sufficient to accurately capture the lattice rotation band parallel to the

11   sliding direction underneath the contact, which is also observed in the TKD

12   experimental results shown in **Figure 11**(b). In addition, the lattice rotation map

13   predicted by the DDP simulations exhibits several thin strips with a limited lattice

14   rotation compared to that in adjacent regions, which separate the lattice rotation band

15   from the subsurface. The separation lines are again interpreted as tracelines (*i.e.* the

16   discontinuity discussed in Section 4.1), and the depths of the first two tracelines are

17   similar to those observed in the TKD pattern map. The DDP simulations not only

18   exhibit a similar lattice rotation pattern, but the predictions also appear to be

19   quantitatively commensurate with the magnitude of misorientation measured

20   experimentally between different material strips shown in **Figure 11**(b). For instance,

21   the lattice rotation within the most severely rotated material strip is roughly $\Omega = 30°$ in

22   the DDP calculations, whereas the relative misorientation measured using TKD

23   between the surface and the region below the second traceline is $\Omega = 25°$. The

24   calculated lattice rotation and misorientation measurement in the other two layers show

25   the same trend. In Section 3.4, we have shown the positive dependence of the lattice

rotation band dimensions on the contact size. The depth of the heavily rotated material enlarges with the contact size and the lattice rotation in the simulations does not extend to the full region shown in **Figure 11**(b) due to the limited contact size used for the simulation. In the experiment the material below the second (lowest) DTL shows large rotation deeper into the substrate (see **Figure 11**b) as the contact size is substantially larger than the field of view in STEM (about one micrometre).

5   Conclusion

Discrete dislocation plasticity analyses have been conducted to simulate the dislocation structure and localized lattice rotation under single asperity sliding, where the contact between the asperity and specimen was established by a preceding sinusoidal indentation. This was done to interpret the dislocation tracelines observed in corresponding experiments. The following conclusions are highlighted:

(i) The entire sliding process up until full slip occurs is divided into three regimes by sliding distance, where the two critical sliding distances demarcating these regimes are identified from the shear stress and dislocation density response. Both of the critical distances are found to be strongly contact size dependent.

(ii) The "dislocation traceline", characterized by an abrupt contrast change observed in the STEM images obtained after the first sliding stroke, is due to a highly localized lattice rotation band within the material subsurface and parallel to the sliding direction, which emerges with increasing sliding distance and is dependent upon the contact size. The lattice rotation arises as a result of the deformation induced by the pattern of concentric dislocation dipoles in conjunction with the compatibility constraint of the surrounding material and the applied contact condition at the surface.

1 (iii) The critical depth from the contact to the top boundary of the horizontal lattice

2 rotation band predicted by the DDP calculations shows excellent agreement with the

3 experimental measurements. Contact size and the corresponding total normal load do

4 not affect the critical depth of the initial traceline, yet these parameters dominate the

5 width and depth of the lattice band when fully slip occurs. This finding provides

6 mechanistic insight into the damage development and subgrain formation observed in

7 tests when larger loads are applied, which have not been explicitly modelled in this

8 contribution.

9 (iv) A very good agreement was observed between the predicted lattice rotation

10 magnitude and the experimentally measured misorientation between subsurface layers.

15 Appendix
16 **Lattice rotation validation for indentation (Supplement to Section 2.3)**
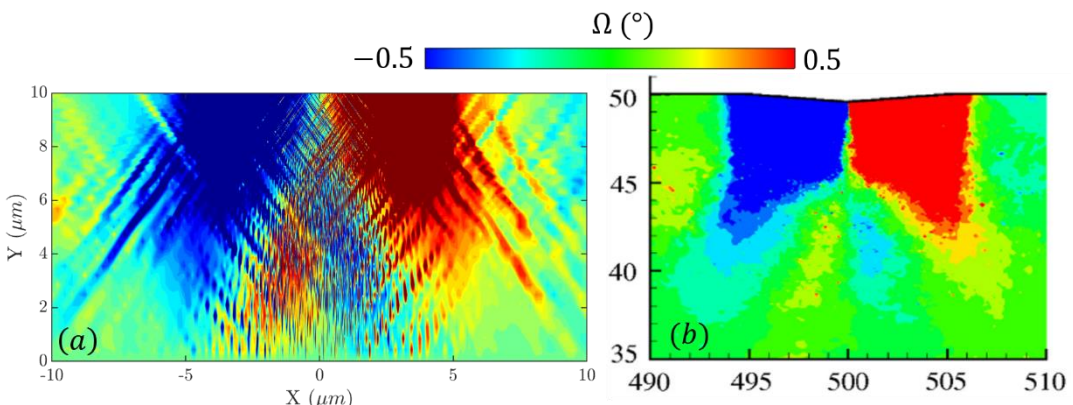
17

18 Figure A 1. Lattice rotation validation for indentation. Lattice rotation distribution in
19 indentation of (a) the sinusoidal indenter adopted in this research (b) a wedge-shaped
20 indenter with similar geometric characteristics studied in (Zhang et al., 2014) . The

1 result is shown at the instant when the same indentation depth $\delta = 0.4$ µm is imposed
2 on both indenters, respectively.

3 **Material properties**

4 Table 1. Material properties in DDP modelling

Parameter Name	Symbol	Unit	Value
Young's modules	E	GPa	70
Poisson ratio	v	-	0.33
Burger's vector	b	nm	0.25
Spacing of slip planes	-	b	100
Drag coefficient	B	Pa·s	10^{-4}
Annihilation distance	L_e	b	6
Mean source strength	$\bar{\tau}_{nuc}$	MPa	50
Obstacle strength	τ_{obs}	MPa	150
Source density	ρ_{nuc}	μm^{-2}	40
Obstacle density	ρ_{obs}	μm^{-2}	80

5

6 **Supplementary Information**

7 VideoS1 shows the lattice rotation development of the film under sliding with contact

8 size A=3.55µm.

9

References

Akarapu, S., Zbib, H.M., Bahr, D.F., 2010. Analysis of heterogeneous deformation and dislocation dynamics in single crystal micropillars under compression. Int J Plasticity 26, 239-257 DOI: http://dx.doi.org/10.1016/j.ijplas.2009.06.005.

Arsenlis, A., Parks, D.M., 1999. Crystallographic aspects of geometrically-necessary and statistically-stored dislocation density. Acta Materialia 47, 1597-1611 DOI: http://dx.doi.org/10.1016/S1359-6454(99)00020-8.

Balint, D.S., Deshpande, V.S., Needleman, A., Van der Giessen, E., 2005. A discrete dislocation plasticity analysis of grain-size strengthening. Mat Sci Eng a-Struct 400, 186-190 DOI: http://dx.doi.org/10.1016/j.msea.2005.02.082.

Balint, D.S., Deshpande, V.S., Needleman, A., Van der Giessen, E., 2006a. Discrete dislocation plasticity analysis of the wedge indentation of films. Journal of the Mechanics and Physics of Solids 54, 2281-2303 DOI: http://dx.doi.org/10.1016/j.jmps.2006.07.004.

Balint, D.S., Deshpande, V.S., Needleman, A., Van der Giessen, E., 2006b. Size effects in uniaxial deformation of single and polycrystals: a discrete dislocation plasticity analysis. Model Simul Mater Sc 14, 409-422 DOI: http://dx.doi.org/10.1088/0965-0393/14/3/005.

Balint, D.S., Deshpande, V.S., Needleman, A., Van der Giessen, E., 2008. Discrete dislocation plasticity analysis of the grain size dependence of the flow strength of polycrystals. Int J Plasticity 24, 2149-2172 DOI: http://dx.doi.org/10.1016/j.ijplas.2007.08.005.

Benzerga, A.A., 2008. An analysis of exhaustion hardening in micron-scale plasticity. Int J Plasticity 24, 1128-1157 DOI: http://dx.doi.org/10.1016/j.ijplas.2007.08.010.

Bertin, N., Sills, R.B., Cai, W., 2020. Frontiers in the Simulation of Dislocations. Annual Review of Materials Research, Vol 50, 2020 50, 437-464 DOI: http://dx.doi.org/10.1146/annurev-matsci-091819015500.

Bouvier, S., Needleman, A., 2006. Effect of the number and orientation of active slip systems on plane strain single crystal indentation. Model Simul Mater Sc 14, 1105-1125 DOI: http://dx.doi.org/10.1088/0965-0393/14/7/001.

Cheng, J.H., Ghosh, S., 2015. A crystal plasticity FE model for deformation with twin nucleation in magnesium alloys. Int J Plasticity 67, 148-170 DOI: http://dx.doi.org/10.1016/j.ijplas.2014.10.005.

Chenje, T.W., Simbi, D.J., Navara, E., 2004. Relationship between microstructure, hardness, impact toughness and wear performance of selected grinding media for

mineral ore milling operations. Mater Design 25, 11-18 DOI: http://dx.doi.org/10.1016/S0261-3069(03)00168-7.

Cheong, K.S., Busso, E.P., Arsenlis, A., 2005. A study of microstructural length scale effects on the behaviour of FCC polycrystals using strain gradient concepts. Int J Plasticity 21, 1797-1814 DOI: http://dx.doi.org/10.1016/j.ijplas.2004.11.001.

Counts, W.A., Braginsky, M.V., Battaile, C.C., Holm, E.A., 2008. Predicting the Hall-Petch effect in fcc metals using non-local crystal plasticity. Int J Plasticity 24, 1243-1263 DOI: http://dx.doi.org/10.1016/j.ijplas.2007.09.008.

Das, S., Hofmann, F., Tarleton, E., 2018. Consistent determination of geometrically necessary dislocation density from simulations and experiments. Int J Plasticity 109, 18-42 DOI: http://dx.doi.org/10.1016/j.ijplas.2018.05.001.

Deshpande, V.S., Balint, D.S., Needleman, A., Van der Giessen, E., 2007. Size effects in single asperity frictional contacts. Model Simul Mater Sc 15, S97-S108 DOI: http://dx.doi.org/10.1088/0965-0393/15/1/S09.

Deshpande, V.S., Needleman, A., Van der Giessen, E., 2004. Discrete dislocation plasticity analysis of static friction. Acta Materialia 52, 3135-3149 DOI: http://dx.doi.org/10.1016/j.actamat.2004.03.018.

Deshpande, V.S., Needleman, A., Van der Giessen, E., 2005. Plasticity size effects in tension and compression of single crystals. Journal of the Mechanics and Physics of Solids 53, 2661-2691 DOI: http://dx.doi.org/10.1016/j.jmps.2005.07.005.

Dunne, F.P.E., Rugg, D., Walker, A., 2007a. Lengthscale-dependent, elastically anisotropic, physically-based hcp crystal plasticity: Application to cold-dwell fatigue in Ti alloys. Int J Plasticity 23, 1061-1083 DOI: http://dx.doi.org/10.1016/j.ijplas.2006.10.013.

Dunne, F.P.E., Wilkinson, A.J., Allen, R., 2007b. Experimental and computational studies of low cycle fatigue crack nucleation in a polycrystal. Int J Plasticity 23, 273-295 DOI: http://dx.doi.org/10.1016/j.ijplas.2006.07.001.

El Ters, P., Shehadeh, M.A., 2019. Modeling the temperature and high strain rate sensitivity in BCC iron: Atomistically informed multiscale dislocation dynamics simulations. Int J Plasticity 112, 257-277 DOI: http://dx.doi.org/https://doi.org/10.1016/j.ijplas.2018.09.002.

Greiner, C., Liu, Z., Strassberger, L., Gumbsch, P., 2016. Sequence of Stages in the Microstructure Evolution in Copper under Mild Reciprocating Tribological Loading. ACS Appl Mater Interfaces 8, 15809-15819 DOI: http://dx.doi.org/10.1021/acsami.6b04035.

Greiner, C., Liu, Z.L., Schneider, R., Pastewka, L., Gumbsch, P., 2018. The origin of surface microstructure evolution in sliding friction. Scripta Materialia 153, 63-67 DOI: http://dx.doi.org/10.1016/j.scriptamat.2018.04.048.

Gurrutxaga-Lerma, B., Shehadeh, M.A., Balint, D.S., Dini, D., Chen, L., Eakins, D.E., 2017. The effect of temperature on the elastic precursor decay in shock loaded FCC aluminium and BCC iron. Int J Plasticity 96, 135-155 DOI: http://dx.doi.org/https://doi.org/10.1016/j.ijplas.2017.05.001.

Gurrutxaga–Lerma, B., Verschueren, J., Sutton, A.P., Dini, D., 2020. The mechanics and physics of high-speed dislocations: a critical review. International Materials Reviews, 1-41 DOI: http://dx.doi.org/10.1080/09506608.2020.1749781.

Hattori, T., Kaneko, Y., Hashimoto, S., 2008. Wear-induced microstructure in Ni/Cu nano-multilayers. J Mater Sci 43, 3923-3930 DOI: http://dx.doi.org/10.1007/s10853-007-2372-5.

Haug, C., Ruebeling, F., Kashiwar, A., Gumbsch, P., Kubel, C., Greiner, C., 2020. Early deformation mechanisms in the shear affected region underneath a copper sliding contact. Nat Commun 11, 839 DOI: http://dx.doi.org/10.1038/s41467-020-14640-2.

Hirth, J.P., Lothe, J., 1982. Theory of dislocations.

Hughes, D.A., Hansen, N., 2001. Graded nanostructures produced by sliding and exhibiting universal behavior. Phys Rev Lett 87, 135503 DOI: http://dx.doi.org/10.1103/PhysRevLett.87.135503.

Johnson, K.L., 1997. Adhesion and friction between a smooth elastic spherical asperity and a plane surface. P Roy Soc a-Math Phy 453, 163-179 DOI: http://dx.doi.org/10.1098/rspa.1997.0010.

Karthikeyan, S., Agrawal, A., Rigney, D.A., 2009. Molecular dynamics simulations of sliding in an Fe-Cu tribopair system. Wear 267, 1166-1176 DOI: http://dx.doi.org/10.1016/j.wear.2009.01.032.

Kiener, D., Guruprasad, P.J., Keralavarma, S.M., Dehm, G., Benzerga, A.A., 2011. Work hardening in micropillar compression: In situ experiments and modeling. Acta Materialia 59, 3825-3840 DOI: http://dx.doi.org/10.1016/j.actamat.2011.03.003.

Kuksenko, V., Roberts, S., Tarleton, E., 2019. The hardness and modulus of polycrystalline beryllium from nano-indentation. Int J Plasticity 116, 62-80 DOI: http://dx.doi.org/10.1016/j.ijplas.2018.12.008.

Kysar, J.W., Saito, Y., Oztop, M.S., Lee, D., Huh, W.T., 2010. Experimental lower bounds on geometrically necessary dislocation density. Int J Plasticity 26, 1097-1123 DOI: http://dx.doi.org/10.1016/j.ijplas.2010.03.009.

Lewandowski, M.J., Stupkiewicz, S., 2018. Size effects in wedge indentation predicted by a gradient-enhanced crystal-plasticity model. Int J Plasticity 109, 54-78 DOI: http://dx.doi.org/10.1016/j.ijplas.2018.05.008.

Liu, Z.L., Patzig, C., Selle, S., Hoche, T., Gumbsch, P., Greiner, C., 2018. Stages in the tribologically-induced oxidation of high-purity copper. Scripta Materialia 153, 114-117 DOI: http://dx.doi.org/10.1016/j.scriptamat.2018.05.008.

Lu, S.J., Zhang, B., Li, X.Y., Zhao, J.W., Zaiser, M., Fan, H.D., Zhang, X., 2019. Grain boundary effect on nanoindentation: A multiscale discrete dislocation dynamics model. Journal of the Mechanics and Physics of Solids 126, 117-135 DOI: http://dx.doi.org/10.1016/j.jmps.2019.02.003.

Lu, X., Dunne, F.P.E., Xu, Y., 2020. A crystal plasticity investigation of slip system interaction, GND density and stored energy in non-proportional fatigue in Nickel-based superalloy. Int J Fatigue 139, 105782 DOI: http://dx.doi.org/10.1016/j.ijfatigue.2020.105782.

Maj, M., Nowak, M., Musial, S., Plocinski, T., 2020. Experimental analysis of material, lattice and plastic rotation during deformation of aluminium multicrystal. Mat Sci Eng a-Struct 790, 139725 DOI: http://dx.doi.org/10.1016/j.msea.2020.139725.

Meissonnier, F.T., Busso, E.P., O'Dowd, N.P., 2001. Finite element implementation of a generalised non-local rate-dependent crystallographic formulation for finite strains. Int J Plasticity 17, 601-640 DOI: http://dx.doi.org/10.1016/S0749-6419(00)00064-4.

Menga, N., Carbone, G., Dini, D., 2018. Do uniform tangential interfacial stresses enhance adhesion? Journal of the Mechanics and Physics of Solids 112, 145-156 DOI: http://dx.doi.org/10.1016/j.jmps.2017.11.022.

Motz, C., Weygand, D., Senger, J., Gumbsch, P., 2008. Micro-bending tests: A comparison between three-dimensional discrete dislocation dynamics simulations and experiments. Acta Materialia 56, 1942-1955 DOI: http://dx.doi.org/10.1016/j.actamat.2007.12.053.

Nix, W.D., Gao, H.J., 1998. Indentation size effects in crystalline materials: A law for strain gradient plasticity. Journal of the Mechanics and Physics of Solids 46, 411-425 DOI: http://dx.doi.org/10.1016/S0022-5096(97)00086-0.

Pastewka, L., Moser, S., Gumbsch, P., Moseler, M., 2011. Anisotropic mechanical amorphization drives wear in diamond. Nat Mater 10, 34-38 DOI: http://dx.doi.org/10.1038/nmat2902.

Peng, B., Li, Q., Feng, X.-Q., Gao, H., 2021. Effect of shear stress on adhesive contact with a generalized Maugis-Dugdale cohesive zone model. Journal of the Mechanics and Physics of Solids 148 DOI: http://dx.doi.org/10.1016/j.jmps.2020.104275.

1 Pharr, G.M., Herbert, E.G., Gao, Y.F., 2010. The Indentation Size Effect: A Critical
2 Examination of Experimental Observations and Mechanistic Interpretations. Annu Rev
3 Mater Res 40, 271-292 DOI: http://dx.doi.org/10.1146/annurev-matsci-070909-104456.

4 Po, G., Huang, Y., Ghoniem, N., 2019. A continuum dislocation-based model of wedge
5 microindentation of single crystals. Int J Plasticity 114, 72-86 DOI:
6 http://dx.doi.org/10.1016/j.ijplas.2018.10.008.

7 Prastiti, N.G., Xu, Y.L., Balint, D.S., Dunne, F.P.E., 2020. Discrete dislocation, crystal
8 plasticity and experimental studies of fatigue crack nucleation in single-crystal nickel.
9 Int J Plasticity 126 DOI: http://dx.doi.org/10.1016/j.ijplas.2019.10.003.

10 Qu, S., Huang, Y., Pharr, G.M., Hwang, K.C., 2006. The indentation size effect in the
11 spherical indentation of iridium: A study via the conventional theory of mechanism-
12 based strain gradient plasticity. Int J Plasticity 22, 1265-1286 DOI:
13 http://dx.doi.org/10.1016/j.ijplas.2005.07.008.

14 Rigney, D.A., Glaeser, W.A., 1978. Significance of near-Surface Microstructure in
15 Wear Process. Wear 46, 241-250 DOI: http://dx.doi.org/10.1016/0043-1648(78)90125-
16 4.

17 Rigney, D.A., Hirth, J.P., 1979. Plastic-Deformation and Sliding Friction of Metals.
18 Wear 53, 345-370 DOI: http://dx.doi.org/10.1016/0043-1648(79)90087-5.

19 Ruebeling, F., Xu, Y., Richter, G., Dini, D., Gumbsch, P., Greiner, C., 2021. Normal
20 Load and Counter Body Size Influence the Initiation of Microstructural Discontinuities
21 in Copper during Sliding. ACS Appl Mater Interfaces DOI:
22 http://dx.doi.org/10.1021/acsami.0c19736.

23 Saraev, D., Miller, R.E., 2006. Atomic-scale simulations of nanoindentation-induced
24 plasticity in copper crystals with nanometer-sized nickel coatings. Acta Materialia 54,
25 33-45 DOI: http://dx.doi.org/10.1016/j.actamat.2005.08.030.

26 Song, H., Deshpande, V.S., Van der Giessen, E., 2016. Discrete dislocation plasticity
27 analysis of loading rate-dependent static friction. Proc Math Phys Eng Sci 472,
28 20150877 DOI: http://dx.doi.org/10.1098/rspa.2015.0877.

29 Sperry, R., Harte, A., da Fonseca, J.Q., Homer, E.R., Wagoner, R.H., Fullwood, D.T.,
30 2020. Slip band characteristics in the presence of grain boundaries in nickel-based
31 superalloy. Acta Materialia 193, 229-238 DOI:
32 http://dx.doi.org/10.1016/j.actamat.2020.04.037.

33 Stoyanov, P., Romero, P.A., Merz, R., Kopnarski, M., Stricker, M., Stemmer, P.,
34 Dienwiebel, M., Moseler, M., 2014. Nano scale sliding friction phenomena at the
35 interface of diamond-like carbon and tungsten. Acta Materialia 67, 395-408 DOI:
36 http://dx.doi.org/10.1016/j.actamat.2013.12.029.

Tarleton, E., Balint, D.S., Gong, J., Wilkinson, A.J., 2015. A discrete dislocation plasticity study of the micro-cantilever size effect. Acta Materialia 88, 271-282 DOI: http://dx.doi.org/10.1016/j.actamat.2015.01.030.

Van der Giessen, E., Needleman, A., 1995. Discrete Dislocation Plasticity - a Simple Planar Model. Model Simul Mater Sc 3, 689-735.

van der Giessen, E., Schultz, P.A., Bertin, N., Bulatov, V.V., Cai, W., Csányi, G., Foiles, S.M., Geers, M.G.D., González, C., Hütter, M., Kim, W.K., Kochmann, D.M., Llorca, J., Mattsson, A.E., Rottler, J., Shluger, A., Sills, R.B., Steinbach, I., Strachan, A., Tadmor, E.B., 2020. Roadmap on multiscale materials modeling. Model Simul Mater Sc 28, 043001 DOI: http://dx.doi.org/10.1088/1361-651X/ab7150.

Widjaja, A., Van der Giessen, E., Deshpande, V.S., Needleman, A., 2007a. Contact area and size effects in discrete dislocation modeling of wedge indentation. J Mater Res 22, 655-663 DOI: http://dx.doi.org/10.1557/Jmr.2007.0090.

Widjaja, A., Van der Giessen, E., Needleman, A., 2007b. Discrete dislocation analysis of the wedge indentation of polycrystals. Acta Materialia 55, 6408-6415 DOI: http://dx.doi.org/10.1016/j.actamat.2007.07.053.

Xu, Y., Balint, D.S., Dini, D., 2016. A method of coupling discrete dislocation plasticity to the crystal plasticity finite element method. Model Simul Mater Sc 24, 045007 DOI: http://dx.doi.org/10.1088/0965-0393/24/4/045007.

Xu, Y., Balint, D.S., Dini, D., 2019. A new hardness formula incorporating the effect of source density on indentation response: A discrete dislocation plasticity analysis. Surf Coat Tech 374, 763-773 DOI: http://dx.doi.org/10.1016/j.surfcoat.2019.06.045.

Xu, Y., Joseph, S., Karamched, P., Fox, K., Rugg, D., Dunne, F.P.E., Dye, D., 2020. Predicting dwell fatigue life in titanium alloys using modelling and experiment. Nat Commun 11, 5868 DOI: http://dx.doi.org/10.1038/s41467-020-19470-w.

Zhang, M., Neu, R.W., McDowell, D.L., 2009. Microstructure-sensitive modeling: Application to fretting contacts. Int J Fatigue 31, 1397-1406 DOI: http://dx.doi.org/10.1016/j.ijfatigue.2009.03.023.

Zhang, Y.H., Gao, Y.F., Nicola, L., 2014. Lattice rotation caused by wedge indentation of a single crystal: Dislocation dynamics compared to crystal plasticity simulations. Journal of the Mechanics and Physics of Solids 68, 267-279 DOI: http://dx.doi.org/10.1016/j.jmps.2014.04.006.